Bottom-up construction of reduced-graphene-oxide-anchored spinel magnet Fe2.02Ni1.01O3.22, anatase TiO2and metallic Ag nanoparticles and their synergy in photocatalytic water reduction

R. Bourzami, M.K. Guediri, D. Chebli, A. Bouguettoucha, Abdeltif Amrane

Bottom-up construction of reduced-Graphene-Oxide-anchored spinel magnet $Fe_{2.02}Ni_{1.01}O_{3.22}$, anatase TiO_2 and metallic Ag nanoparticles and their synergy in photocatalytic water reduction

Riadh BOURZAMI[a*], Mohamed Khalil GUEDIRI[b], Derradji CHEBLI[b], Abdallah BOUGUETTOUCHA[b], Abdeltif AMRANE[c]

[a] Research unit of emergent materials, Ferhat Abbas, Sétif-1 university, Sétif, Algeria

[b] Département de Génie des Procédés, Laboratoire de Génie des Procédés Chimiques, Faculté de Technologie, Université Ferhat Abbas, Sétif-1, 19000 Sétif, Algérie

[c] Univ Rennes, Ecole Nationale Supérieure de Chimie de Rennes, CNRS, ISCR – UMR6226, F-35000 Rennes, France

E-mail : abdeltif.amrane@univ-rennes1.fr

* Corresponding author, E-mail: ***riadh_bourzami@hotmail.com***

Abstract

Paramagnet spinel $NiFe_2O_4$ nanocrystals were synthesized using the hydrothermal route and were put in contact with anatase TiO_2 PC500; the mixture of semi-conductors was employed as substrate to deposit reduced Graphene Oxide (rGO) sheets synthetised via Hummers modified method. Several rGO mass amounts 'x' were deposited (x = 0, 5, 10, 15% and 20%). These steps of synthesis were followed by surface decoration with Ag metallic particles using the photodeposition method, wich led to different heterojunction nanocomposite materials. The XRD analysis proved that the $NiFe_2O_4$ has a spinel crystalline structure and the anatase TiO_2 has a tetragonal system; these crystalline systems were conserved after the deposition of rGO. The electronic properties were studied experimentally using the UV-Vis DRS illustrating a hierarchical gap for the spinel $NiFe_2O_4$ and an indirect gap for TiO_2; these analyses revealed that the electronic and structural properties are affected when the rGO is deposited. The SEM images proved the formation of the heterojunction and the good mixing of $NiFe_2O_4$ and TiO_2 with the rGO. The EDX allowed attributing a chemical formula for the spinel structure, $Fe_{2.02}Ni_{1.01}O_{3.22.}$ Furthermore, the photocatalytic properties are influenced by the specific area of the photocatalyst; for that the DLS analysis was carried out to estimate the average aggregated grain seize. At the end, the composites were evaluated for their enhanced adsorptive performance and photocatalytic activity under visible light irradiation to degrade Methylene Blue (MB). In addition, the deposit of metallic Ag showed great improvement in the photocatalytic performances over pristine composites.

Graphical abstract

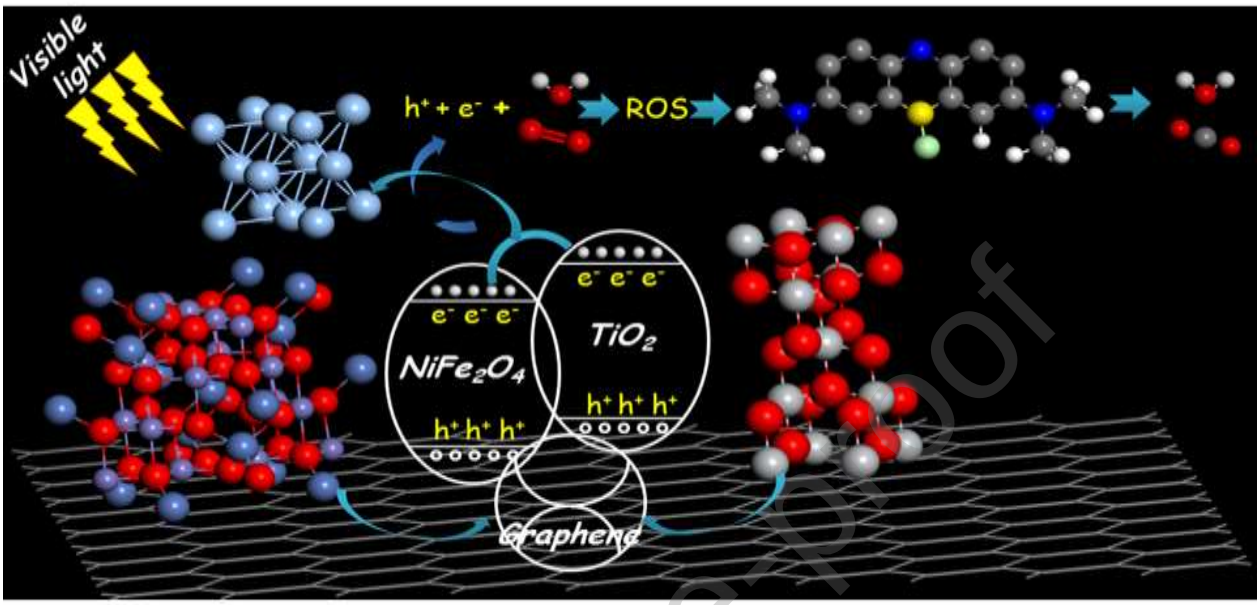

Keywords: Spinel, $NiFe_2O_4$, TiO_2, heterojunction, reduced Graphene Oxide rGO, photocatalysis.

1. **Introduction**

Non-biodegradable or recalcitrant organic pollution have today become crucial environmental problems because of their toxicities and persistence. Refractory organic products, mainly generated by industries are continuously discharged into waterways or the environment. A large quantity of wastewater from the textile industry contains dyes of various kinds whose elimination by conventional biological processes turns out to be ineffective. Thus, adsorption materials have found an importance in environmental processes [1-3], but with these materials, pollution is only transferred from the liquid phase to the solid phase [4]. Consequently, it is necessary to find a new material having high catalytic power, which is not only capable to destroy pollutants into simpler and above all biodegradable compounds. In this way, many researchers have tried to synthesize new heterogeneous photocatalysts based on nanoparticles metallic oxides [5,6].

As a new carbon material considered as an ideal support for nanoparticles [7], discovered in 2004, graphene has a two-dimensional (2D) structure and has a thickness of only one atom. It aroused extraordinary interest, thanks to its physical properties. Graphene has been widely used

in several fields [8-10], owing to its high surface area, excellent electronic conductivity in storage and transport of electrons and high mechanical resistance [11,12]. In addition, graphene oxide (GO) can be easily functionalized in order to modify its physical properties [13], rGO can be obtained by reduction of GO by electrical, chemical or thermal treatments [14,15].

The fixation of metal oxide nanoparticles on graphene or its derivatives including graphene oxide and carbon nanotube have shown their effectiveness as adsorbent and in photocatalysis [16-19]. It is noted that the carbonic materials prevent the aggregation of nanoparticles immobilized on their surface.

The metal oxides of structures AB_2O_4, A and B are divalent and trivalent metal cations respectively, are called spinel compounds and they can be indexed regarding the X-ray diffraction analysis as cubic face-centered with Fd3m space group [20-23], in which, 1/8 of tetrahedral sites and 1/2 of octahedral sites are occupied by A and B cations respectively. This family of compounds has attracted considerable attention in few recent years, owing to their narrow band gaps and their great visible-light responses in wastewater treatment.

Among the spinel composite oxide compounds, the spinel ferrite nanoparticles MFe_2O_4 (where M is divalent metal) have a vast potential for several technological applications [24,25], because of their optical-electrical properties, magnetic properties and mechanical and chemical stabilities [26, 27]. They have been used in adsorption, photocatalysis, hydrogen in solar cells, magnetostrictive sensors, transducers, actuators, supercapacitors, Li-ion batteries, drug delivery, memory devices, microwave and spintronic devices, catalysis and gas sensor [28-31]. From that, several researchers have synthesized nanoparticles of MFe_2O_4 by different techniques, such as micro-emulsion method, co-precipitation method, sol-gel auto-combustion method, hydrothermal method, solvothermal method, etc. [32-35]. Among the spinel ferrite nanoparticles, the $NiFe_2O_4$ spinel has shown good magnetic properties, allowing an easy separation, and it also shows an interesting photocatalytic activity [36]. In this context, only few researches on $NiFe_2O_4$ were developed in the fields of elimination of organic pollutant by photocatalytic processes [37,38]. Other than that, $NiFe_2O_4$ nanoparticles were used for reduction of metals [39], hydrogen production, reduction of CO_2 and photoelectrochemical water splitting [40,41]. Other researchers have synthesized spinel-LDH composites for the adsorption and photocatalysis [42].

In order to increase the photocatalytic activity of spinels by separating the photogenerated e-hole couple [43, 44], some researchers have synthesized nanocomposites of $NiFe_2O_4$ deposited on

two-dimensional structure materials, such as g-C_3N_4 as well as on other photocatalytic semiconductors such as ZnO and TiO_2 [45-47]. Other researchers have introduced other materials into the $NiFe_2O_4$-TiO_2 matrix, such as polypropylene, silica and ionic liquids [48].

This study focused therefore on the development of the photolytic properties of $NiFe_2O_4$, by adopting three strategies. The first one was the production of the junction $NiFe_2O_4$-TiO_2; the second one was the deposition of rGO on $NiFe_2O_4$-TiO_2 and the last one was the deposition of metallic Ag nanoparticules; synthesizing finally the $NiFe_2O_4$-TiO_2/rGO/Ag composite. The photocatalytic activities of $NiFe_2O_4$-TiO_2, $NiFe_2O_4$-TiO_2/rGO and $NiFe_2O_4$-TiO_2/rGO/Ag were compared; the systematic structural and electronic characterizations were also performed.

2. Experimental part

2.1. Materials and methods

2.1.1. Preparation of Graphene Oxide (GO)

GO was synthesized by the modified Hummers method [49]. In a typical synthesis, 5 g of powder graphite and 2.5 g of potassium nitrate $K(NO_3)$ were added to 115 mL of 98% sulfuric acid H_2SO_4 and mixed with constant stirring; the temperature of the mixture was kept below 10 °C using an ice bath. 15 g of potassium permanganate $KMnO_4$ was slowly added to the suspension and the stirring was continued for 2 h. Next, the temperature was increased to 35 °C and the mixture was kept at this temperature for another 45 min. Further, 230 mL of distilled water was added dropwise to the paste; the temperature was increased up to 98 °C and the reaction was maintained for 45 min. Finally, the resulted suspension was further diluted with addition of 350 mL of warm distilled water H_2O, and then treated with 15 mL of H_2O_2 (30%) solution to reduce the residual permanganate; the addition of H_2O_2 resulted in a yellow color, indicating high level of oxidation and the manganese dioxide swing to colorless soluble manganese sulfate. The suspension was washed with 5% HCl aqueous solution using centrifuge until total removal of SO_4^{-2}. The removal of SO_4^{-2} was detected by addition of barium chloride, since the presence of sulfate ion induced a white precipitate when barium chloride was added to the supernatant [50]. Then, the mixture was repeatedly centrifuged and washed with de-ionized water until the pH of the supernatant was neutral. Finally, the material was dried at 40 °C for 72 h giving brown black sample.

2.1.2. Preparation of $NiFe_2O_4$

0.02 mol of $Ni(NO_3)2.6H_2O$, 0.04 mol of $Fe(NO_3)_3.9H_2O$ (the Ni^{2+}/Fe^{3+} molar ratio was 1/2) and 5 g of PEG (Poly Ethylene Glycol) in 20 ml of 50% aqueous alcohol were added in 100 ml water. PEG was added to obtain small homogeneous particle size; after 10 minutes of stirring, the aqueous NaOH solution was added successively dropwise with continuous stirring until the pH reached 11.

Then, the precursor solution was treated by sonication for 30 minutes and transferred to a hydrothermal stainless steel reactor for 12 h of hydrothermal treatment at 190 °C. It was then cooled to room temperature. The resulting product was collected by centrifugation, then washed with deionized water and ethanol several times, then dried under vacuum. The last step was calcination at 600 °C for 4 h.

2.1.3. Preparation of $NiFe_2O_4$-TiO_2

Commercial TiO_2 PC500, with an average particle size of 25 nm, was chosen as precursor in the preparation of $NiFe_2O_4$-TiO_2 junction. The composite consisted of a mass ratio of 5 % $NiFe_2O_4$ and 95 % TiO_2; this molar ratio corresponded to 0.08 g of $NiFe_2O_4$ and 1.52 g of TiO_2. For this purpose, they were suspended in 40 ml ethanol, with subsequent addition of 0.25 g of maleic acid; the mixture was maintained under stirring vigorously for 2 h. The suspension was collected by centrifugation and washed several times with water and ethanol and was dried overnight in air at 60 °C, and finally annealed at 230 °C for 3 h.

2.1.4. Preparation of $NiFe_2O_4$-TiO_2/rGO

The preparation of $NiFe_2O_4$-TiO_2/rGO photocatalysts with different weight ratios 5, 10, 15 and 20 wt.% of rGO to $NiFe_2O_4$-TiO_2 were prepared via the hydrothermal method. 200 mg of $NiFe_2O_4$-TiO_2 powder and appropriate mass percent of GO were dispersed in solution of H_2O (40 ml) and ethanol (20 ml); the mixture was treated by ultrasonic waves for 2 h and stirred for another 2 h to obtain homogenous suspension. The suspension was transferred to Teflon sealed autoclave and maintained at 120 °C for 12 h. The resulting compound was washed several times by centrifugation in distilled water and ethanol and finally, dried in an oven at 60 °C for 24 h.

2.2. Materials characterization

2.2.1. XRD

The XRD analysis was performed using a diffractometer X'Pret PANalytical equipped with Cu anticathode characterized by an incident wavelength $K_{\alpha 1}$(λ = 1,5406 Å). The acceleration tension

was fixed at de 40 kV and the courant at 30 mA; the scan step was about 0.016 ° with an accumulation time of 0.2 s per step, in the range of 5 ° to 90 °.

2.2.2. DLS

Hydrodynamic diameter was measured using Dynamic Light Scattering (DLS) of the type Horiba Patrica LA960, equipped with capillary cell.

2.2.3. SEM

The morphology was investigated with Scanning Electron Microscopy (SEM) of the type FEI QUANTA 250 FEG (FEI, Hillsboro, OR, USA), with 10 KV as acceleration voltage.

2.2.4. FTIR

Infrared Fourier Transform (FT-IR) analyzes were carried out on an Agilent Technologies 4300-Spectrophotometer in the region between 4500 and 500 cm^{-1}.

2.2.5. UV-Vis-DRS

Optical transmission and absorption spectra were performed in Ultraviolet-Visible Diffuse Reflection Spectroscopy (UV-Vis-DRS) spectrometer, Shimadzu UV-3600 spectrophotometer with a Harrick Praying Mantis accessory, in the range of 200 to1000 nm.

2.3. Adsorption Kinetics

The adsorption kinetic curves allow determining the time necessary to obtain the adsorption equilibrium [51]. The procedure was carried out in the dark and at room temperature as follows: 50 mg $NiFe_2O_4$-TiO_2/rGO_x (x = 0, 5, 10, 15 and 20%) was dispersed in a 200 ml solution of MB with a concentration of 10 mg/L; it was rigorously stirred. To follow the evolution of the adsorbed quantity (Q_{ads}), samples were taken at time intervals of 10 min until equilibrium was obtained. The yield was calculated according to the relation (1):

$$R(\%) = \frac{(C_0 - C_e)}{C_0} \times 100 \quad (1)$$

Where R is the percentage of MB fixed on the adsorbent, C_0 the initial concentration of the MB solution (mg/L) and C_e the residual concentration of the MB solution at equilibrium (mg/L).

2.3.1. Equilibrium modeling

The study of adsorption dynamics describes solute adsorption rate. This rate controls the residence time of adsorbed molecules on the solid–solution interface. Several kinetic models were applied to fit experimental data [51]. In this work, three models were used: pseudo-first-order,

pseudo-second order and pseudo n^{th} order. The conformity of the experimental results with those of the modeling was estimated by the correlation coefficients R^2.

2.3.1.a. Pseudo First Order model (PFO)

The PFO kinetic model is the study of the adsorption into solid/liquid interface; this model is based on the adsorption capacity [51, 52] and managed by the relation (2):

$$\frac{dQ_t}{dt} = k_1 (Q_e - Q_t) \quad (2)$$

Where Q_e (mg/g) and Q_t (mg/g) refer to the amount of dye adsorbed at equilibrium and at time t (min) respectively, k_1 (min^{-1}) is the equilibrium rate constant.

The solution of the differential equation Eq.2, with the following boundary conditions t = 0 to t = t and $Q_t = 0$ to Q_t gives relation (3):

$$Q_t = Q_e(1 - e^{-K_1 t}) \quad (3)$$

2.3.1.b. Pseudo Second Order model (PSO)

The PSO model is applicable to a wider time interval, usually the entire adsorption process [52]. This model is governed by the relation (4):

$$Q_t = \left(\frac{k_2 {Q_e}^2 t}{k_2 Q_e t + 1}\right) \quad (4)$$

Where k_2 ($g.mg^{-1}\ min^{-1}$) is the equilibrium rate constant of PSO model.

2.3.1.c. Pseudo n^{th} Order ($Pn^{th}O$)

The general rate law equation without pre-set order to a fixed value can be written as (relation (5) [51, 52]:

$$\frac{dQ_t}{dt} = K_n (Q_e - Q_t)^n \quad (5)$$

The solution of the differential equation Eq.5, with the boundary conditions gives the relation (6):

$$Q_t = Q_e\left(1 - \frac{1}{\left[1+(n-1)K_n t {Q_e}^{(n-1)}\right]^{\frac{1}{n-1}}}\right) \quad (6)$$

Where R is the percentage of MB fixed on the adsorbent, C_0 the initial concentration of the MB solution (mg/L) and C_e the residual concentration of the MB solution at equilibrium (mg/L).

2.4. Photocatalytic tests

Photocatalytic experiments were monitored using Shimadzu 1700 UV-Vis. spectrophotometer. The spectra were recorded between 200 and 800 nm and the kinetic curves were traced for the absorbance at λ_{max} = 664 nm of the MB.

Photocatalytic tests were performed at room temperature, using visible Xenon light (two lamps of 150 W), placed at 30 mm above an open-air beaker with exposed surface to LED light of about 32.17 cm^2. MB was chosen as the model molecule for photo-degradation experiments due to its easy availability and its wide use in industry. The procedure was performed as follows: 30 mg of $NiFe_2O_4$-TiO_2/rGO_x (x = 0, 5, 10, 15 and 20%) were dispersed in 200 ml of aqueous solution of MB (10 mg/L); the natural pH was about 6.5. Firstly, the solution was stirred in the dark for 70 min, in order to establish the adsorption desorption equilibrium. After 70 min, each 15 min, 1 ml of the suspension was taken and immediately centrifuged to separate the catalyst from the solution, and then analyzed by UV-Vis. spectroscopy.

3. Results and discussion

3.1. Characterization

3.1.1. XRD

The Figure 1 shows the XRD patterns of TiO_2, $NiFe_2O_4$ and $NiFe_2O_4$-TiO_2/rGO_x (x = 0, 5, 10, 15 and 20%). Several diffraction peaks can be seen on the diffractograms for TiO_2 at the angular positions: 2θ = 25.24°, 37.87°, 47.98°, 54.54°, 62.57°, 69.70°, 75.21° and 82.78°. These peaks were attributed according to the reference pattern (96-900-8215) as respectively (1 0 1), (0 0 4), (2 0 0), (1 0 5), (2 0 4), (1 1 6), (2 1 5) and (2 2 4) Bragg's planes of anatase structure, which has a tetragonal system. For $NiFe_2O_4$ at the angular positions 2θ = 18.40°, 30.25°, 35.69°, 37.30°, 43.30°, 44.50°, 53.89°, 57.28°, 62.99°, 71.59° and 74.45°, the peaks were attributed according to the reference pattern (96-100-6117) as respectively (1 0 1), (0 0 4), (2 0 0), (1 0 5), (2 0 4), (1 1 6), (2 1 5) and (2 2 4) Bragg's planes of cubic system. No new peaks were observed for $NiFe_2O_4$–TiO_2 in comparison with those of $NiFe_2O_4$ and TiO_2, indicating the absence of any chemical reaction between the two pristine compounds.

For the composites, the mass ratio of $NiFe_2O_4$ to TiO_2 was 5% to 95 %, leading to a weak apparition of the peaks relative to $NiFe_2O_4$ in the composite patterns, which are marked by only three first intense peaks (022), (131) and (101) (mentioned by a star *).

It can be seen also from the XRD-patterns that more the ratio of rGO sheets was high more the XRD-patterns appeared noisy, indicating the presence of amorphous phase of rGO.

Furthermore, the diffraction peaks of the composites shifted comparatively to the peaks of $NiFe_2O_4$-TiO_2, when mass ratio "x" of rGO increased toward the great angles, which indicates that the cell parameters were affected during the deposit, leading to the generation of a stress in the crystalline structure. The comparison of the cell parameter measures of $NiFe_2O_4$, TiO_2, and in their junction are summarized in the Table 1, and the variations of the cell parameters with the increase of rGO ratio are illustrated in the Figure 2. The characteristic cell parameters are calculated using the relations (7):

$$2d_{hkl}\sin\theta = n\lambda \quad \text{and} \quad d_{hkl} = \frac{1}{\sqrt{\frac{h^2}{a^2}+\frac{k^2}{b^2}+\frac{l^2}{c^2}}} \qquad (7)$$

With d_{hkl}: the interreticular spacing, K = 0.94 constant of the form, β: the width at half-height and θ is the angle of diffraction.

It is seen from the values of the Table 1 that the cells of $NiFe_2O_4$ and TiO_2 were dilated when they were attached; the dilation rate $\frac{\Delta a}{a} = \frac{a-a_0}{a_0}$ was 0.056 % for cubic $NiFe_2O_4$ and the $\frac{\Delta a}{a}$ and $\frac{\Delta c}{c}$ values for TiO_2 were 0.229 % and 0.614 %. Those values indicate that the junction of the two semiconductors induced a significant dilation of the TiO_2 especially along the direction 'c', while the cell of $NiFe_2O_4$ was almost unchangeable.

The cell parameter measures were calculated for both crystalline phases of $NiFe_2O_4$ and TiO_2, but because the weak intensity of the peaks of $NiFe_2O_4$, the grain seize (D), microconstraint (ε%) and the density of the dislocations (δ) were estimated and discussed only for TiO_2, they were calculated according to the relations (1), (8), (9) and (10) [53, 54]. The results are summarized in the Table 1 and the variations of the grain seize (D), the microconstraint (ε%) with the ratio x are illustrated in the Figure 3:

$$D = \frac{K\lambda}{\beta\cos\theta} \qquad (8)$$

$$\varepsilon\% = \frac{\beta}{4\tan\theta} \qquad (9)$$

$$\delta = \frac{1}{D^2} \qquad (10)$$

It is clearly observed from the Figure 2 and the Figure 3, that the fixation of graphene sheets on $NiFe_2O_4$-TiO_2 at the microscopic scale decreased the lattice parameter measures and increased

the microconstraints; and at the macroscopic scale, it reduced the grain seize and induced strong structural defects estimated by a rise of the density of the dislocation.

3.1.2. EDX

In the focus to know the chemical formula of the synthetized $NiFe_2O_4$ compound, EDX analysis was exploited. The EDX spectrum (Figure 4) illustrated the presence of only O, Fe and Ni elements, which confirmed the purity of the compound, with the weight percent of 23.42 %, 49.97 % and 26.61 % (wt. %) respectively. Those values corresponded to atomic fractions, 51.54 %, 32.31 % and 16.15 % and the empiric formula can be written as $Ni_{1.01}Fe_{2.02}O_{3.22}$.

3.1.3. SEM

The Figure 5 shows the SEM images of $NiFe_2O_4$-TiO_2/rGO_x. The images of the first line of the table were captured at weak zoom (x100); they illustrate that the particles of $NiFe_2O_4$ had a strong tendency to form aggregated clusters, which were destroyed when the $FeNi_2O_4$ was joined to TiO_2. Regarding the composites $NiFe_2O_4$-TiO_2/rGO_x (x = 0, 5, 10, 15 and 20%), the images at weak zoom showed a homogenous distribution of $NiFe_2O_4$-TiO_2 particles on the graphene sheets, with a considerable diminution of the aggregation.

The second line of the table shows images captured with the zoom of (x10000); they focalized on the particles of $NiFe_2O_4$-TiO_2, illustrating that the particles had an intermediate shape between spherical and cubic forms. The images of the third line proved the existence of a contact at the microscopic scale between $NiFe_2O_4$-TiO_2 and graphene sheets, confirming the formation of the heterojunction. Otherwise, the fourth line proves the formation of the junction between $NiFe_2O_4$ and TiO_2 with related focalized EDX spectra.

3.1.4. DLS

The photocatalytic reactivity is controlled by the external surface state of the particles. Indeed, the surface exposed to the external media is the surface of the aggregated particles; the aggregation of transition metal oxides in aqueous solution is well known [55, 56]. For this reason, the semiconductor particle of $NiFe_2O_4$ and $NiFe_2O_4$-TiO_2 were characterized by DLS.

The Figure 6 shows the distributions of the hydrodynamic diameter of aggregated nanoparticles in distilled water suspension, showing the formation of various sizes of aggregated particles; the experimental data were fitted with a Gaussian function.

The fitted curve shows that the average seize value of hydrodynamic diameter were 839.29 ± 1.67 nm and 1847.39 ± 4.96 nm and the width at half height of the fitted curve were 251.89 ±

3.39 nm and 631.65 ± 9.79, for $NiFe_2O_4$ and $NiFe_2O_4$-TiO_2 respectively. Those results indicate that both compounds had a great tendency to form aggregated particles; this tendency was more considerable for Fe_2NiO_5 than for the junction $NiFe_2O_4$-TiO_2.

3.1.5. UV-DRS

The catalysis is influenced by the structural and electronic properties of the external surfaces and the interfaces of the compounds. Consequently, strong correlation is obvious between structure, charge-carrier lifetimes and interfacial charge transfer with the adsorption and the photocatalytic activities. More precisely, the light absorption characteristics (i.e., absorption coefficient, band gap energy and Urbach energy) of $NiFe_2O_4$ and $NiFe_2O_4$-TiO_2/rGO_x (x = 0, 5, 10, 15 and 20 %) are critical factors affecting the photocatalytic activity; the UV-Vis-DRS spectroscopy is a suitable tool for studying these properties. The corresponding spectra are shown in the Figure 7. The line of $NiFe_2O_4$ exhibited a large adsorption band in the visible domain overlapped by many small bumps, interpreting thereby a complicate electronic character. In addition, spectroscopic studies revealed a hierarchy of band gaps in both spin up and down channels. The band hierarchical gap refers to the presence of multiple charge gaps in the optical absorption spectrum 57, 58; its large absorption band can be attributed to the transition from the highest occupied bands formed by both Ni3d and O2p to the lowest unoccupied band formed principally by Fe states. The small bumps can be analyzed in the optical data in terms of metal-to-metal intersite d-d and p-d charge-transfer-like excitations [59].

The choice of the $NiFe_2O_4$ was essential, if we take into consideration its hierarchical gap in both up and down channel; in such case, the electron transfer can occur in many ways between the $NiFe_2O_4$, TiO_2 and rGO.

Moreover, the spectra of the composites were mostly dominated by the adsorption of the TiO_2 anatase [60, 61], showing an adsorption band in the UV domain. This adsorption band was due to the electronic transition from the valence band related to the O2p orbitals, followed by Ti4s orbitals, to the conduction band related to the Ti3d, followed by the O2p orbitals [62]. It is seen also from the spectra of the composites that the intensity of the large band in the visible domain increased with the increase of rGO ratio ‘x’, this band was due to the adsorption of the graphene, which was superimposed with the adsorption of the small amount of $NiFe_2O_4$. The adsorption of the composites in the visible light overlapped well with the solar spectrum; an interesting photocatalytic activity can be therefore predicted.

The absorption coefficients 'α' were deduced from the reflectance curves 'R', according to the Kubelka-Munk formula (11) [63, 54]:

$$\alpha = \frac{(1-R)^2}{2R} \quad (11)$$

The band gap 'E_g' was evaluated through the 'Tauc plot' on linear part of $(\alpha.h\gamma)^n \propto (h\gamma\text{-}E_g)$, where n = 2 for the direct gap (Figure 8 (b)) and n = 1/2 for the indirect gap (Figure 8 (a)). The synthetized $NiFe_2O_4$ had energy values of 2.9 and 2.5 eV for n = 2 and n = 1/2 respectively, which were in good agreement with those found in literature (59) (64). For the studied composites, the decrease of the gap was not well defined with the increase of the ratio 'x'; it was found 3.59 to 3.68 eV and from 3.87 to 3.90 eV, for the indirect and direct gap energy respectively.

Another characteristic parameters, which can be evaluated and discussed through the UV-Vis-DRS is the Urbach energy 'E_U'. This energy characterizes the variation in the electronic band structure caused by different origins (vacant or interstitial sites, lattice strain, dislocation…); it characterizes additional states within the band gap near HOMO and LUMO levels, and can be seen as tails of conduction and valence bands. E_U is roughly equal to the average width of tails [65].

The Urbach energy E_U is evaluated using the relation (10) [66]:

$$\alpha = \alpha_0 \exp\left(\frac{h\upsilon - E_0}{E_u}\right) \quad (12)$$

Where, α_0 and E_0 are constants relative to the studied compounds.

'E_U' was estimated through the plot of (lnα) *vs* (hυ) and it was evaluated from the slope of the linear part: $(\ln\alpha) \propto (h\alpha\text{-}E_0)$ (Figure 8 (c)). Contrarily to the gap values, the increase of the values of the Urbach energy was well observed; it increased with the increase of the ratio 'x' from 216 to 386 meV. This increase indicated that the deposit of rGO_x sheets on $NiFe_2O_4$-TiO_2 induced an increase of defects in the crystalline structure, in good agreement with the XRD results that showed an increase of the dislocation density 'δ'. The tails of Urbach shifts the Fermi level; this shift may strengthens the migration of photogenerated electrons and represses the recombination electron-hole, which let expect an improvement of the photocatalytic activity.

3.2. Adsorption activity

The study of adsorption dynamics describes solute adsorption rate. This rate controls the residence time of adsorbed molecules on the solid–solution interface. The Figure 9 shows the experimental points of the adsorption of MB as a function of time and the corresponding fitted

curves with PFO, PSO and PNO models. The experimental values of the adsorption quantities and the results of the fits are summarized in the Table 2. It can be concluded from the fit curves that the saturation of adsorption was obtained after 40 min; to ensure saturation, 70 min equilibrium time was therefore considered. In addition, the adsorbed quantity at saturation increased significantly with the increase of rGO rate 'x' (from Q_{ads} = 14.59 mg/g to Q_{ads} = 25.40 mg/g), due to the high specific area of the graphene.

According to the Table 2, the adsorbed quantities Q_{ads} calculated with the PFO model were not close to the experimental values; while those given by the PSO model were much closer. In addition, the precision of the adjustment was generally better seen through the correlation coefficients R^2. R^2 values were between 0.888-0.981, 0.956-0.997 and 0.983-0.994 for the PFO, PSO and PNO models, respectively. According to the results obtained concerning the correlation coefficients R^2, we can rule out the PFO model, which led to the lowest correlation coefficients.

A statistical factor has been recently introduced to choose the most suitable correlation model; it is the Akaike Information Criterion (AIC). A comparison of the kinetic models was also carried out considering the AIC and the results are summarized in the Table 3.

The AIC measures the quality of statistical models; it was proposed in 1973 by Hirotugu Akaike. Thus, the AIC must be minimal to minimize the loss of information. The model proposed was implemented for the description of the experimental data points of the dye adsorption. The ideal adjustment is obtained when the R^2 are high and the AIC values are low. The general form for calculating the AIC is given by the formula (13) [67, 68].

$$AIC = 2K - Ln\left(\frac{SSR}{n-k}\right) \quad (13)$$

Where: k is the number of data points, RSS is the residual sums of squares and n is number of parameters.

Also, the AIC can be deduced by introducing the chi-square of fitting [69] by the expression (14):

$$AIC = x^2 + 2p \quad (14)$$

Where p is the number of parameters of the fitted model, x^2 is the chi-square.

According to the results summarized in the Table 3, it seems that the PSO model gave the best results concerning the AIC (lowest values) for $NiFe_2O_4$-TiO_2/rGO_x (x = 5%, x = 10%, x = 15% and x = 20%), although the R^2 values were comparable to those obtained by the PNO model. It

can also be pointed out that the AIC for $NiFe_2O_4$-TiO_2/rGO_x (x = 0% and x = 20%) showed that the PNO model was more suited to represent the absorption of MB on semiconductor composites ($NiFe_2O_4$-TiO_2/rGO_x). It can also be noted that the AIC values for the $NiFe_2O_4$-TiO_2/$rGO_{0\%}$ were very close, AIC = -22.95 and AIC = -23.38 for PSO and PNO models, respectively. The PFO model was therefore discarded because it gave low R^2 and large AIC compared to the PSO and PNO models. Overall, the PSO model can be considered as the most appropriate to represent the MB adsorption mechanism on the different composites.

To identify the adsorption mechanism, the effect of resistance to intra-particulate scattering on adsorption was evaluated by the intra-particulate scattering model expressed by the mathematic relation (15):

$$Q = k_{id} * t^{0.5} + C \quad (15)$$

The values of the external diffusion constant k_{id} obtained after the first 5 minutes, as well as R^2 are given in the Table 4. From the Figure 10, it is easy to see that the intra-particle diffusion is an important step in the process of adsorption of MB on the various composites used in this work.

The plot of Q(t) as a function of the square root of time $t^{0.5}$, in the time interval ranging from 5 to 30 min of contact between the MB and the different composites, is displayed in Figure 10. In this time interval, the straight lines showed that the adsorption process of MB on the composites was in the zone, which corresponds to the diffusion in the macropores and the transport of the dye molecules from the solution to the surface of the adsorbent. This lag time in adsorption can be explained by the displacement of the dye molecules in the channels of the $NiFe_2O_4$-TiO_2 particles, before reaching the surface.

However, the surface adsorption process, which begins from the first minutes of contact and whose experimental points were well represented by the PSO model with very good regression coefficients R^2, indicates that the intraparticle diffusion step was limiting, and hence controlled the transfer rate of MB at each instant t. The results obtained for the K_{id} showed a maximal value of this constant for the $NiFe_2O_4$-TiO_2/$rGO_{10\%}$ composite.

3.3. Photocatalytic activity

The photo-degradation of the MB by $NiFe_2O_4$-TiO_2/rGO_x (x = 0, 5, 10, 15 and 20 %) composites was followed by UV-Visible spectroscopy. The Figure 11 shows the decay of normalized concentration ($C(t)/C_0$) recorded at λ = 664 nm, and the kinetic points are fitted by an exponential fuction according to the relation (16):

$$\frac{C(t)}{C_0} = A_0 + B_0 e^{-k_{ap}t} \quad (16)$$

Where: A_0 is undegraded rest, A_0+B_0 gives the initial point at t = 0 and k_{ap} is the apparent rate constant of photocatalysis, the fit curves are superimposed on the Figure 11, and the constant rates calculated considering the linear regression are summarized in the Table 5.

To better compare the effect of adsorption and photocatalysis, the histograms displayed in Figure 12 show their yields of elimination. Comparatively to the others, the composite x = 10% gave a high constant rate, 8.62 mn^{-1}, as well as a high removal yield by photocatalysis, 36.19%. Owing to the good yields of elimination by adsorption and photocatalysis, the composite x = 10% was chosen as substrate for the decoration by metallic Ag nanoparticles, in order to improve the elimination of MB. Two amounts of metallic Ag were considered, 1% and 4%. Comparatively to $NiFe_2O_4$-TiO_2/$rGO_{10\%}$, the deposit of metallic Ag enhanced well the photocatalytic activity; the constant rates were 9.52 and 17.88 mn^{-1} and the elimination yields were improved by 21% and 26% for $Ag_{1\%}$ and $Ag_{4\%}$ respectively. Otherwise, the synthetized composites have a good yield of elimination, and can be considered as a good photocatalysts compared to other photocatalytic systems based on metal-oxyde/graphene composites [70], for example, M. K. Guediri and al. found a total yield of elimination about 45 % for $FeTiO_3$/$rGO_{10\%}$ [71]. In addition, the $NiFe_2O_4$-TiO_2/rGO_x can be easily separated by centrifuging from the reaction systems without mass loss of the catalysts, to guarantee the recyclability of the photocatalysts, the photocatalytic tests were performed in three cycles and no obvious decrease of catalytic reduction activity was remarked, however, the recyclability of metal and metal oxide/graphene is well known [72,73].

Moreover, the UV-Visible spectroscopy proves the good photocatalytic performance of the synthetized composites, but, it cannot prove the complete mineralization of the MB molecules, this is related to the fact that, the photodegradation of the dyes may induce the formation of colorless unstable transition products, especially in the presence of dissolved molecular oxygen [70].

3.4. Proposed mechanism

The histograms (Figure 12) illustrate that the yield of the photocatalytic process was influenced by the addition of graphene. In other words, the graphene not only increased the adsorption but is also involved in the electronic transfer during photocatalysis. This latter can act through different ways:

(i) The rGO π-conjugated electrons system favors thermodynamically the generation of ROS (Reactive Oxygen Species), and can oxidizes directly MB, and creates additional photocatalytic active sites in the composites [74-75]; (ii) thanks to its gap null, rGO shifts the adsorption to the high wavelength and increases the absorption in the visible region, increasing the photogenerated carriers quantity; and (iii) rGO works as 'p' part (receiver) in the p-n junction ($NiFe_2O_4$-TiO_2 as donor), the electrons photogenerated on $NiFe_2O_4$-TiO_2 surfaces tend to be transferred to rGO sheets, which enhances the lifetime of the photogenerated charge carrier.

The choice of the $NiFe_2O_4$ is essential if we take into consideration its hierarchical gap in both the up and down channels; in such case, the electron transfer can occur in many electronic ways between the $NiFe_2O_4$, TiO_2 and rGO.

The addition of metallic Ag increased considerably the elimination yield. This can be explained by the extension of the lifetime of photogenerated carriers; when Ag is deposited on the surface of the semiconductor ($NiFe_2O_4$-TiO_2/$rGO_{10\%}$) (Schottky junction), at the interface, the band states of the metallic Ag are deeply buried into the band states of semiconductors [75]. In such situation, two parameters of the semiconductor must raise the work function of the electrons in the semiconductors and the Fermi level [63]. Furthermore, when the semiconductor is excited, the electrons of the CB flow into the Ag metal until equilibrium that is achieved when the Fermi energies are the same for both the metal and the semiconductor. The electron transfer to the metal delays the recombination electron-hole and increases the reactivity of electrons with the external media, enhancing thereby the photocatalytic performances. The Figure 13 summarizes the different proposed ways of the electron transfer in the composites.

4. **Conclusion**

A series of $NiFe_2O_4$-TiO_2/rGO_x nanocomposites with various graphene amounts were successfully synthesized using a facile hydrothermal method to form heterojunction composites.

The XRD analysis proved that the $NiFe_2O_4$ had a spinel crystalline structure and the anatase TiO_2 had a tetragonal system. These structures are conserved after the deposition of rGO, although the crystalline size and the cell parameters decreased, evidently accompanied by an increase of the microconstraints (ξ%); this induced strong structural defects estimated by an increase of the dislocation density (δ). Furthermore, SEM images proved the formation of the heterojunction and the good mixing of $NiFe_2O_4$ and TiO_2 with the rGO.

The gap of pristine $NiFe_2O_4$ is hierarchical; this property offers to the composites many channels for the electron transfer. The UV-Vis-DRS spectroscopy revealed, though the Tauc formula, a direct gap of 2.9 eV and an indirect gap value of 2.2 eV. Owing to the presence of the anatase TiO_2, the composites had a strong absorption in the UV domain, and the graphene extended the absorption in the visible giving a good absorption in all the electromagnetic spectrum. This characteristic offered to the composites good photosensing ability. The gap values given by the Tauc formula was similar to the gap of anatase TiO_2; its change was not well defined, while the increase of the Urbach energy with the increase of the ratio x was well observed from 216 to 386 meV.

Moreover, the adsorption kinetic curves showed that the amount of MB adsorbed increased with the increase of the rGO amount, with an equilibrium time of approximately 40 minutes. The fit of the kinetic curves proved that the pseudo second order model was adequate. The photocatalytic study showed that all synthetized compounds had an impact on the degradation of the MB under visible light; the junction with rGO sheets improved considerably the adsorptive and photocatalytic performances and the best synergy between the two ways of elimination was obtained for the $NiFe_2O_4/rGO_{10\%}$ composite. The results indicated that deposit of graphene and decoration with Ag metallic particles enhanced visible light absorption and greatly improved separation of photogenerated carriers; the sample $NiFe_2O_4$-$TiO_2/rGO_{10\%}@Ag_{4\%}$ exhibited the best photocatalytic performances. At the end, a mechanism of photocatalysis was proposed.

Acknowledgment

Authors are thankful to the General Directorate of Scientific Research and Technological Development (DGRSDT) and the University Ferhat Abbes, Setif-1.

References

1. S. Farhadi, F. Siadatnasab "nanocomposite: Preparation, characterisation, and application in sonocatalytic degradation of organic dye pollutants" Chin. J. Catal., 37 (2016) 1487–1495.

2. S. Karthikeyan, V. K. Gupta, R. Boopathy, A. Titus, G. Sekaran "A new approach for the degradation of high concentration of aromatic amine by heterocatalytic Fenton oxidation: Kinetic and spectroscopic studies" J. Mol. Liq., 173 (2012) 153-163.

3. Y. Liu, C. Luo, J. Sun, H. Li, Z. Sun, S. Yan "Enhanced adsorption removal of methyl orange from aqueous solution by nanostructured proton-containing δ-MnO_2" J. Mater. Chem. A, 3 (2015) 5674–5682.

4. D. Chebli, F. Fourcade, S. Brosillon, S. Nacef, A. Amrane "Supported photocatalysis as a pre-treatment prior to biological degradation for the removal of some dyes from aqueous solutions, Acid Red183, Biebrich Scarlet, Methyl Red Sodium Salt, Orange II" J. Chem. Technol. Biotechnol., 85 (2010) 555-563.

5. L. Xia, B. Li, Y. Zhang, R. Zhang, L. Ji, H. Chen, G. Cui, H. Zheng, X. Sun, F. Xie, Q. Liu "Cr_2O_3 Nanoparticle-Reduced Graphene Oxide Hybrid: A Highly Active Electrocatalyst for N2 Reduction at Ambient Conditions" Inorg. Chem., 58 (2019) 2257-2260.

6. J. Qian, Z. Chen, F. Chen, Y. Wang, Z. Wu, W. Zhang, Z. Wu, P. Li "Exploration of CeO_2–CuO Quantum Dots in Situ Grown on Graphene under Hypha Assistance for Highly Efficient Solar-Driven Hydrogen Production" Inorg. Chem., 57 (2018) 14532-14541.

7. Y. Zhu, S. Murali, W. Cai, X. Li, J. W. Suk, J. R. Potts, R. S. Ruoff. "Graphene and Graphene Oxide: Synthesis, Properties, and Applications" Adv. Mater., 22 (2010) 3906-3924.

8. K. S. Novoselov, A. K. Geim, S. V. Morozov, D. Jiang, Y. Zhang, S. V. Dubonos, I. V. Grigorieva, A. A. Firsov "Electric Field Effect in Atomically Thin Carbon Films" Science, 306 (2004) 666-669.

9. S. Chen, J. Zhu, X. Wang "From Graphene to Metal Oxide Nanolamellas: A Phenomenon of Morphology Transmissio" ACS Nano., 4 (2010) 6212-6218.

10. A. Khort, V. Romanovski, V. Lapitskaya, T. Kuznetsova, K. Yusupov, D. Moskovskikh, Y. Haiduk, K. Podbolotov "Graphene@Metal Nanocomposites by Solution Combustion Synthesis" Inorg. Chem., 59 (2020) 6550-6565.

11. A. K. Geim, K. S. Novoselov "The rise of graphene" Nat. Mater., 6 (2007) 183-191.

12. L.-b. Tang, B. Zhang, C.-S. An, H. Li, B. Xiao, J.-H. Li, Z.-J. He, J.-C Zheng. "behavior anode materials of $MoSe_2$ Nanosheets anchored on dual-heteroatoms functionalized Graphene for sodium-ion batteries" Inorg. Chem., 58 (2019) 8169-8178.

13. Y. Zhu, S. Murali, W. Cai, X. Li, J. W. Suk, J. R. Potts, R. S. Ruoff "Graphene and Graphene Oxide: Synthesis, Properties, and Applications" Adv. Mater., 22 (2010) 3906–3924.

14. A. T. Habte, D. W. Ayele. "Synthesis and Characterization of Reduced Graphene Oxide (rGO) Started from Graphene Oxide (GO) Using the Tour Method with Different Parameters" Adv. Mater. Sci. Eng., 9 (2019) 1-9.

15. U. Wang, H. Wu, Z. Liu, H. Zhao, H. Liu, Y. Zhan "Bottom-Up Construction of Reduced-Graphene-Oxide-Anchored MnO with an Nitrogen-Doped Carbon Coating for Synergistically Improving Lithium-Ion Storage" Inorg. Chem., 57 (2018) 13693-13701.

16. Y. Fu, H. Chen, X. Sun, X. Wang "Graphene-supported nickel ferrite: A magnetically separable photocatalyst with high activity under visible light" AIChE J., 58 (2011) 3298–3305.

17. Y. Men, X. Liu, F. Yang, F. Ke, G. Cheng, W. Luo. "Carbon Encapsulated Hollow Co_3O_4 Composites Derived from Reduced Graphene Oxide Wrapped Metal–Organic Frameworks with Enhanced Lithium Storage and Water Oxidation Properties" Inorganic Chemistry, 57 (2018) 10649-10655.

18. M. Feliz, P. Atienzar, M. Amela-Cortés, N. Dumait, P. Lemoine, Y. Molard, S. Cordier. "Supramolecular Anchoring of Octahedral Molybdenum Clusters onto Graphene and Their Synergies in Photocatalytic Water Reduction" Inorg. Chem., 58 (2019) 15443-15454.

19. J. Zhang, X. Wang, Y. Xue, Z. Xu, J. Pei, Z. Zhuang. "Self-Assembly Precursor-Derived MoP Supported on N, P-Codoped Reduced Graphene Oxides as Efficient Catalysts for Hydrogen Evolution Reaction" Inorg. Chem., 57 (2018) 13859-13865.

20. T. Tatarchuk, B. Al-Najar, M. Bououdina, M. Abdel Aal Ahmed Springer International Publishing AG 2018 L. M. T. Martínez and al. (eds.), Handbook of Ecomaterials,.

21. S. M. Ismail, M. Yehia, S. S. Ata-Allah. "Hydrothermal synthesis of strontium-doped ZnS nanoparticles: structural, electronic and photocatalytic investigations" Bull. Mater. Sci., 42 (2019) 223-230.

22. S. Joshi, M. Kumar, S. Chhoker, G. Srivastava, M. Jewariya, V.N. Singh. "Structural, magnetic, dielectric and optical properties of nickel ferrite nanoparticles synthesized by co-precipitation method" J. Mol. Struct., 1076 (2014) 55-62.

23. H. Bi, F. He, Y. Dai, J. Xu, Y. Dong, D. Yang, S. Gai, L. Li, C. Li, P. Yang. "Quad-Model Imaging-Guided High-Efficiency Phototherapy Based on Upconversion Nanoparticles and $ZnFe_2O_4$ Integrated Graphene Oxide" Inorg. Chem., 57 (2018) 9988-9998.

24. S. Kamali "Spin structure, magnetism and cation distributions of $NiFe_{2-x}Al_xO_4$ solid solutions" J. Magn. Magn. Mater., 433 (2017) 155-161.

25. R. Zhang, Q. Yuan, R. Ma, X. Liu, C. Gao, M. Liu, C.-L. Jia, H. Wang. "Tuning conductivity and magnetism of $CuFe_2O_4$ via cation redistribution" RSC Adv., 7 (2017) 21926-21379.

26. R Boulkroune, M Sebais, Y Messai, R Bourzami, M Schmutz, C Blanck, O Halimi, B Boudine "Influence of Zinc Doping on the Structural and Magnetic Properties of Ni-Ga-Sm Polycrystalline Ferrites" J. Supercond. Nov. Magn., 28 (2015) 2875-2880.

27. B. V. Prasad, K. V. Ramesh, A. Srinivas. "Structural and Magnetic Studies of Nano-crystalline Ferrites MFe_2O_4 (M = Zn, Ni, Cu, and Co) Synthesized Via Citrate Gel Autocombustion Method" J. Supercond. Nov. Magn., 30 (2017) 3523-3535.

28. A. Kovalenko, R. S. Yadav, J. Pospisil, O. Zmeskal, D. Karashanova, P. Heinrichova , M. Vala, J. Havlica, M. Weiter. "Towards improved efficiency of bulk-heterojunction. Solar cells using various spinel ferrite magnetic nanoparticles" Org. Electron., 39 (2016) 118-126.

29. P. N. Anantharamaiah, P. A. Joy. "Tuning of the magnetostrictive properties of cobalt ferrite by forced distribution of substituted divalent metal ions at different crystallographic sites" J. Appl. Phys., 121 (2017) 93904-93915.

30. R. S. Yadav, J. Havlica, M. Hnatko, P. Šajgalík, C. Alexander, M. Palou, E. Bartonícková, M. Bohác, F. Frajkorová, J. Masilko, M. Zmrzlý, L. Kalina, M. Hajdúchová, V. Enev. "Magnetic properties of $Co_{1-x}Zn_xFe_2O_4$ spinel ferrite nanoparticles synthesized by starch-assisted sol–gel autocombustion method and its ball milling" J. Magn. Magn. Mater., 378 (2015) 190-199.

31. R. S. Yadav, J. Havlica, J. Masilko, L. Kalina, M Hajdúchová, V. Enev, J. Wasserbauer, I. Kuritka, Z. Kožáková. "Structural, Cation Distribution, and Magnetic Properties of $CoFe_2O_4$ Spinel Ferrite Nanoparticles Synthesized Using a Starch-Assisted Sol-Gel Auto-Combustion Method" J. Supercond. Nov. Magn., 28 (2015) 1851-1868.

32. P. Guo, L. Cui, Y. Wang, M. Lv, B. Wang, X. S. Zhao. "Facile Synthesis of $ZnFe_2O_4$ Nanoparticles with Tunable Magnetic and Sensing Properties" Langmuir, 28 (2013) 8997−9003.

33. A. Kamzina, A. Bingolbalib, N. Doğanc, Z. Yeşild, M. Asiltürke "The Magnetic Structure of $NiFe_2O_4$ Nanoparticles" Appl. Phys. Lett., 45 (2019) 1008-1011.

34. J. Tan, W. Zhang, A.-L. Xia "Facile synthesis of inverse spinel $NiFe_2O_4$ nanocrystals and their superparamagnetic properties" *Mater. Res,* 16 (2013) 237-241.

35. J. L. Gunjakar, A. M. More, K. V. Gurav, C. D. Lokhande "Chemical synthesis of spinel nickel ferrite ($NiFe_2O_4$) nano-sheets" Appl. Surf. Sci., 254 (2008) 5844-5848.

36. K. Raj, R. Moskowitz "Commercial applications of ferrofluids" J. Magn. Magn. Mater., 85 (1990) 233-245.

37. A. Ren, C. Liu, Y. Hong, W. Shi, S. Lin, P. Li "Enhanced visible-light-driven photocatalytic activity for antibiotic degradation using magnetic $NiFe_2O_4/Bi_2O_3$ heterostructures" Chem. Eng. J., 258 (2014) 301-308.

38. S. Gautam, P. Shandilya, V. P. Singh, P. Raizada, P. Singh "Solar photocatalytic mineralization of antibiotics using magnetically separable $NiFe_2O_4$ supported onto graphene sand composite and bentonite" J. Water Process. Eng., 14 (2016) 86-100.

39. M. O. Ojemaye, O. O. Okoh, A, I. Okoh "Uptake of Zn^{2+} and As^{3+} from wastewater by adsorption onto imine functionalized magnetic nanoparticles" water, 10 (2018) 36-54.

40. R. Dillert, D. H. Taffa, M. Wark, T. Bredow, D. W. Bahnemann "Research Update: Photoelectrochemical water splitting and photocatalytic hydrogen production using ferrites (MFe_2O_4) under visible light irradiation" APL Mater., 3 (2015) 104001-104015.

41. S. Chandrasekarana, C. Bowenc, P. Zhanga, Z. Lid, Q. Yuana, X. Rena, L. Denga "Spinel photocatalysts for environmental remediation, hydrogen generation, CO_2 reduction and photoelectrochemical water splitting" J. Mater. Chem. A, 6 (2018) 11078-11104.

42. C. D. Valencia-Lopez, M. Zafra-Calvo, M. J. Martín de Vidales, V. Blanco-Gutierrez, E. Atanes-Sanchez, N. Merayo, F. Fernandez-Martinez, A. Nieto-Marquez, A. J. Dos santos-Garcia "Synthesis of $NiFe_2O_4$-LDH Composites with High Adsorption and Photocatalytic Activity for Methyl Orange Degradation" Inorganics, 6 (2018) 98-107.

43. D. Zhang, X. Pu, Y. Gao, C. Su, H. Li, H. Li, W. Hang "One-step combustion synthesis of $CoFe_2O_4$–graphene hybrid materialsfor photodegradation of methylene blue" Mater. Lett., 113 (2013) 179-181.

44. S. Balaji, R. Kalai Selvan, L. John Berchmans, S. Angappan, K. Subramanian, C. O. Augustin "Combustion synthesis and characterization of Sn^{4+} substituted nanocrystalline $NiFe_2O_4$" Mater. Sci. Eng. B, 119 (2005) 119-124.

45. B. Palanivel, C. Ayappan, V. Jayaraman, S. Chidambaram, R. Maheswaran, A. Mani "Inverse spinel $NiFe_2O_4$ deposited g-C_3N_4 nanosheet for enhanced visible light photocatalytic activity" Mater. Sci. Semicond. Process, 100 (2019) 87-97.

46. D. Q. Hung, N. K. Thanh "Preparation of $NiFe_2O_4$-TiO_2 nanoparticles and study of their photocatalytic activity" VNU J. Sci. Mathermatics – Physics, 27 (2011) 204-211.

47. R. Yeni, S. Arief, Y. Stiadi, R. Rizal, Z. Zulhadjri "Synthesis of magnetic nanoparticles of TiO_2-$NiFe_2O_4$: Characterization and photocatalytic activity on degradation of rhodamine B" Indo. J. Chem., 12 (2012) 229-234.

48. A. Vasanthakumar, G. G. Redhi, R. M. Gengan "Efficient catalytic activity of ionic liquid-supported $NiFe_2O_4$ magnetic nanoparticle doped Titanium Dioxide nano-composite" Int. J. Chem. Eng. Appl., 7 (2016) 422-427.

49. R. D. Kumar, R. Thangappan, R. Jayavel "Facile Preparation of $LaFeO_3$/rGO Nanocomposites with Enhanced Visible Light Photocatalytic Activity" J. Inorg. Organomet. P., 27 (2017) 892-900.

50. T. F. Emiru, D. W. Ayele "Controlled synthesis, characterization and reduction of graphene oxide: A convenient method for large scale production" Egyp. Jour. Bas. App. Sci., 4 (2017) 74-79.

51. D. Chebli, A. Bouguettoucha, T. Mekhalef, S. Nacef, A. Amrane "Valorization of an agricultural waste, Stipa tenassicima fibers, by biosorption of an anionic azo dye, Congo red" Desalin. Water. Treat., 54 (2015) 245-254.

52. A. Bouguettoucha, A. Reffas, D. Chebli, T. Mekhalif, A. Amrane "Novel activated carbon prepared from an agricultural waste, Stipa tenacissima, based on $ZnCl_2$ activation-characterization and application to the removal of methylene blue" Desalin. Water. Treat., 57 (2016) 24056–24069.

53. I. A. Abdel-Latif, A. A. Ismail, M. Faisal, A. M. Ali, A. E. Al-Salmi, A. Al-Hajry "Impact of the annealing temperature on perovskite strontium doped neodymium manganites nanocomposites and their photocatalytic performances" J. Taiwan. Inst. Chem. E, 75 (2017) 174-182.

54. Z. Huang, X. Dai, Z. Huang, T. Wang, L. Cui, J. Ye, P. Wu "Simultaneous and efficient photocatalytic reduction of Cr(VI) and oxidation of trace sulfamethoxazole under LED light by rGO@Cu_2O/$BiVO_4$ p-n heterojunction composite" Chemosphere, 221 (2019) 824–833.

55. D. Jassby, J. Farner Budarz, M. Wiesner "Impact of Aggregate Size and Structure on the Photocatalytic Properties of TiO_2 and ZnO Nanoparticles" Environ. Sci. Technol., 46 (2012) 6934-6941.

56. J. Melcher, N. Barth, C. Schilde, A. Kwade, D. Bahnemann "Influence of TiO_2 agglomerate and aggregate sizeson photocatalytic activity" J. Mater. Sci., 52 (2016) 1047-1056.

57. Q.-C. Sun, H. Sims, D. Mazumdar, J. X. Ma, B. S. Holinsworth, K. R. O'Neal, G. Kim, W. H. Butler, A. Gupta, and J. L. Musfeldt " Optical band gap hierarchy in a magnetic oxide: Electronic structure of $NiFe_2O_4$" Phys. Rev. B, 86 (2012) 205106-205110.

58. H.-T. Jeng, G. Y. Guo "First-principles investigations of the magnetocrystalline anisotropy in strained Ni-substituted magnetite ($NiFe_2O_4$)" J. Magn. Magn. Mater., 240 (2002) 436–438.

59. Y. Zhang, J. He, Q. Yang, H. Zhu, Q. Wang, Q. Xue, L. Yu "Solution quenched in-situ growth of hierarchical flower-like $NiFe_2O_4/Fe_2O_3$ heterojunction for wide-range light absorption" J. Power Sources, 440 (2019) 227120-227126.

60. Youcef Messai, Bertrand Vileno, David Martel, Philippe Turek, Djamel Eddine Mekki "Milling effect on the photo-activated properties of TiO_2 nanoparticles: electronic and structural investigations" Bull. Mater. Sci., 41 (2018) 57-68.

61. D. Eder, M. Motta and A. H. Windle "Iron-doped Pt–TiO_2 nanotubes for photo-catalytic water splitting" Nanotechnology, 20 (2009) 055602-055608.

62. E. Araujo-Lopez, L. A. Varilla, N. Seriani, J. A. Montoya "TiO_2 anatase's bulk and (001) surface, structural and electronic properties: a DFT study on the importance of Hubbard and van der Waals contributions" Surf. Sci., 653 (2016) 187–196.

63. P. M. Nithya, L. G. Devi "Effect of surface Ag metallization on the photocatalytic properties of $BaTiO_3$: Surface plasmon effect and variation in the Schottky barrier height" Surf. Interfaces, 15 (2019) 205-215.

64. S. N. Dolia, R. Sharma, M. P. Sharma, N. S. Saxena "Synthesis, X-ray diffraction and optical band gap study of nanoparticles of $NiFe_2O_4$" Indian J. pure and appl. phys., 44 (2006) 774-776.

65. B. Choudhury, M. Dey, A. Choudhury "Defect generation, d-d transition, and band gap reduction in Cu-doped TiO_2 nanoparticles" Int. Nano Lett., 3 (2013) 25-33.

66. The physics of semiconductors—an introduction including (Heidelberg, Berlin: Springer). Grundmann, M. 2010.

67. O. M. Unuabonah, E. I. Akpa "Small-sample corrected Akaike information criterion: an appropriate statistical tool for ranking of adsorption isotherm models" Desalination, 272 (2011) 20-26.

68. M. H. El-Naas, M. A. Alhaija, S. Al-Zuhair "Evaluation of an activated carbon packed bed for the adsorption of phenols from petroleum refinery wastewater" Environ. Sci. Pollut. Res., 24 (2017) 7511-7520.

69. M. BenYahia, S. Knani, L. BenHajHsan, M. BenYahia, H. Nasri, A. BenLamine "Statistical studies of adsorption isotherms of iron nitrate and iron chloride on a thin layer of porphyrin" J. Mol. Liq., 248 (2017) 235–245.

70. Y. -H. Chiu, T. -F. M. Chang, C. -Y. Chen, M. Sone, Y. -J. Hsu "Mechanistic Insights into Photodegradation of Organic Dyes Using Heterostructure Photocatalysts, Graphene-based heterojunction photocatalysts" Catalysts, 9 (2019) 430-462.

71. M. K. Guediri, D. Chebli, A. Bouguettoucha, R. Bourzami, A. Amrane "Novel Fe_2TiO_5/reduced graphene oxide heterojunction photocatalyst with improved adsorption capacity and visible light photoactivity: experimental and DFT approach" Environ. Sci. Pollut. Res., 28 (2021) 8507–8519.

72. W. Liu, Z. Li "Assembly of RGO composite aerogels embedded with ultrasmall Au nanoparticles as an active and recyclable catalyst for reduction of 4-nitrophenol" J. Environ. Chem. Eng., (2020) in press.

73. F. Bu, I. Shakir, Y. Xu "3D Graphene Composites for Efficient Electrochemical Energy Storage" Adv. Mater. Interfaces, 5 (2018) 1800468-1800490.

74. X. Jiang, J. Nisar, B. Pathak, J. Zhao, R. Ahuja "Graphene oxide as a chemically tunable 2-D material for visible-light photocatalyst applications" J. Catal., 299 (2013) 204-209.

75. Y. Li, X. Wu, W. Ho, K. Lv, Q Li, M. Li, S. C. Lee "Graphene-Induced Surface Vacancy of Zn_2SnO_4 for the Enhanced Visible-Light-Driven Photocatalytic Oxidation of NO and Acetone oxidation" Chem. Eng. J., 336 (2018) 200-210.

74. S. Wan, M. Chen, M. Ou, Q. Zhong "Plasmonic Ag nanoparticles decorated $SrTiO_3$ nanocubes for enhanced photocatalytic CO_2 reduction and H_2 evolution under visible light irradiation" J. CO_2 Util., 33 (2019) 357–364.

Figure Captions

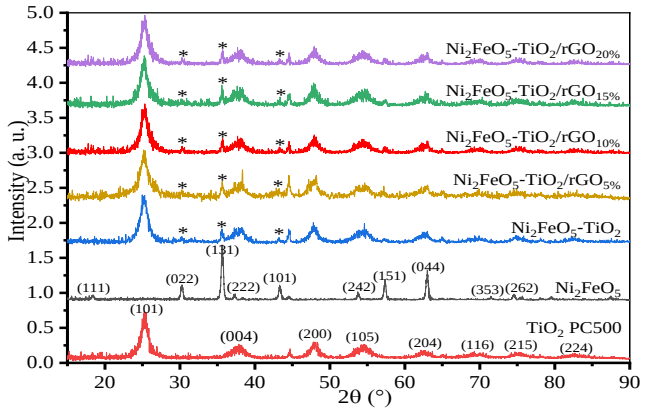

Figure 1. Diffraction patterns of TiO_2, $NiFe_2O_4$ and $NiFe_2O_4$-TiO_2/rGO_x (x = 0, 5, 10, 15 and 20%).

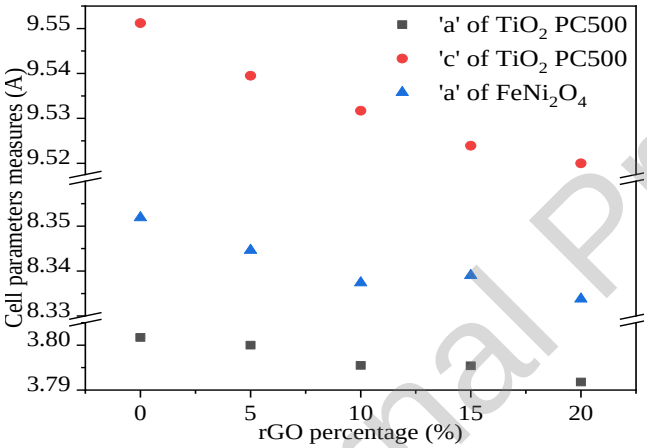

Figure 2. Cell parameter measures.

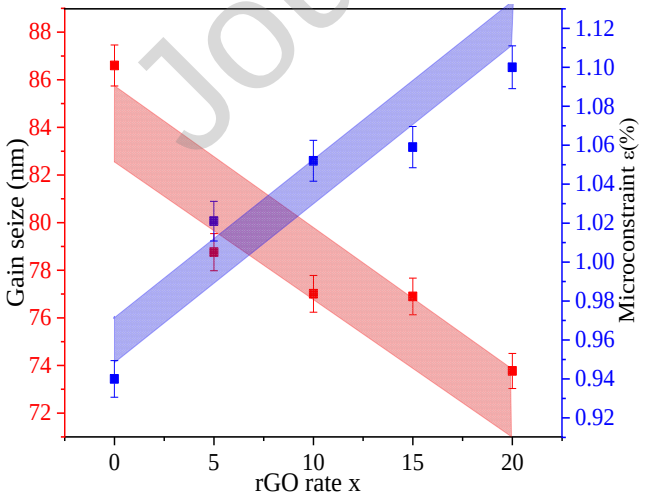

Figure 3. Variation of grain sizes and microconstraints vs rGO rate x.

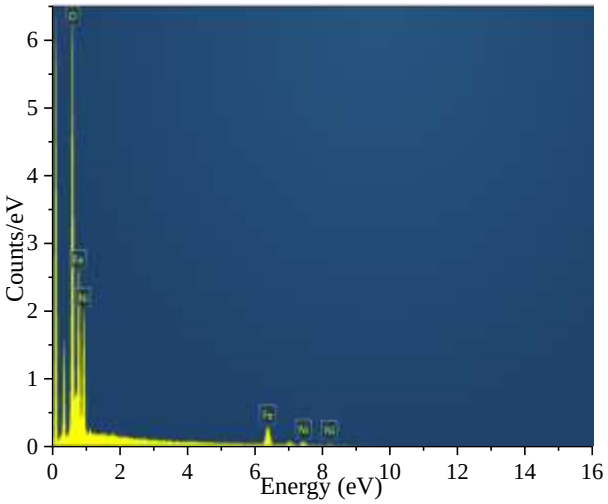

Figure 4. EDX spectrum of $NiFe_2O_4$.

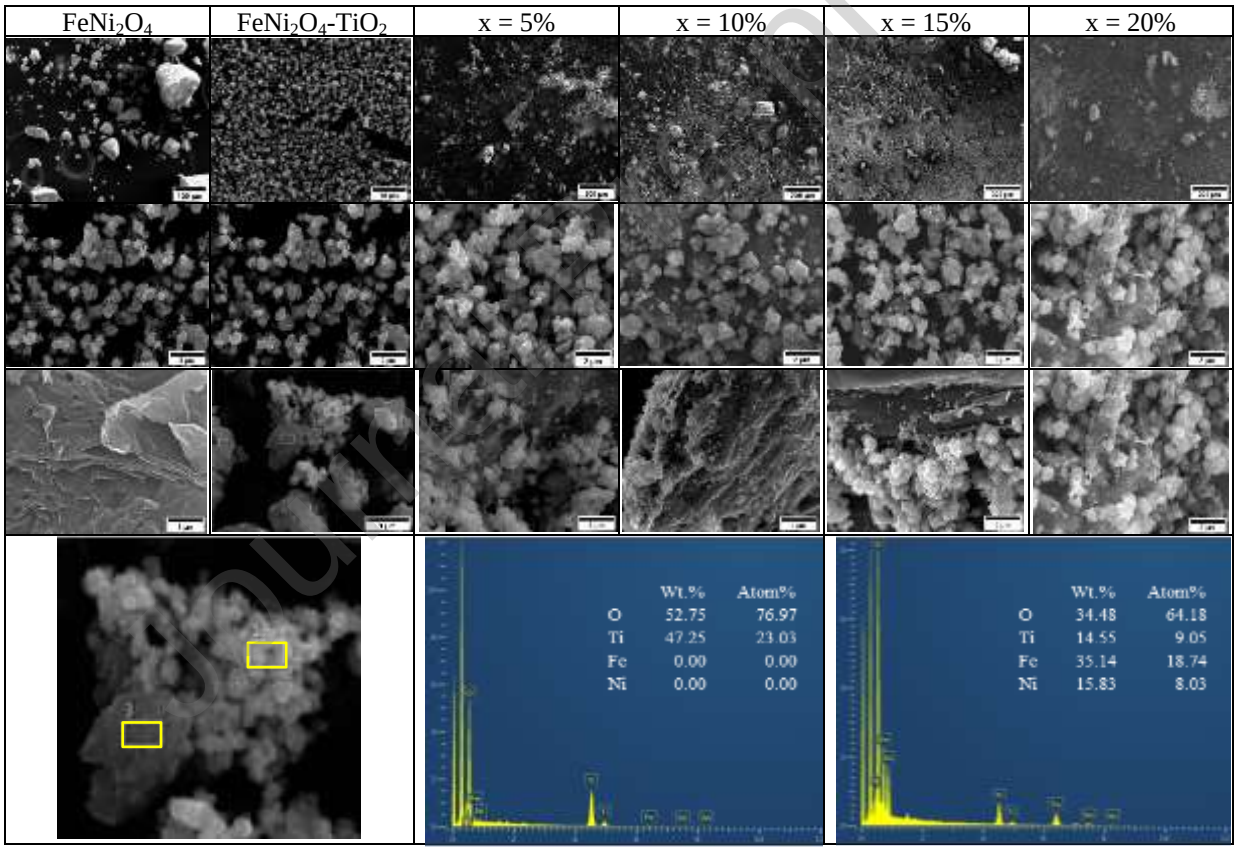

Figure 5. SEM images, first line: weak zoom x100, middle and third-line strong zoom x10000 for $NiFe_2O_4$ and $NiFe_2O_4$-TiO_2/rGO_x (x = 0, 5, 10, 15 and 20%).

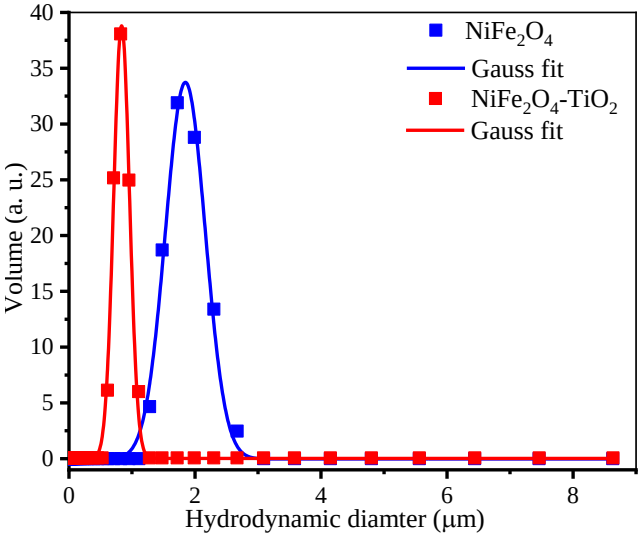

Figure 6. Hydrodynamic diameter of $NiFe_2O_4$ and $NiFe_2O_4$-TiO_2 in H_2O suspension, (experimental results: independent points, fit curves: continuous lines).

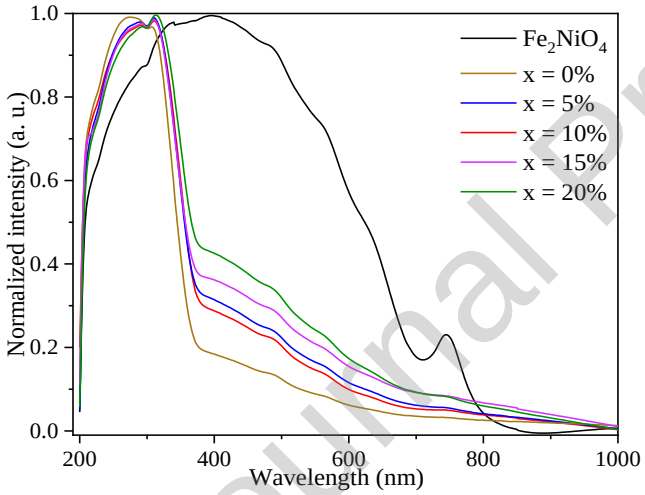

Figure 7. UV-Visible spectra of $NiFe_2O_4$ and $NiFe_2O_4$-TiO_2/rGO_x (x = 0, 5, 10, 15 and 20%). All spectra are normalized to 1 by the maximum of absorbance.

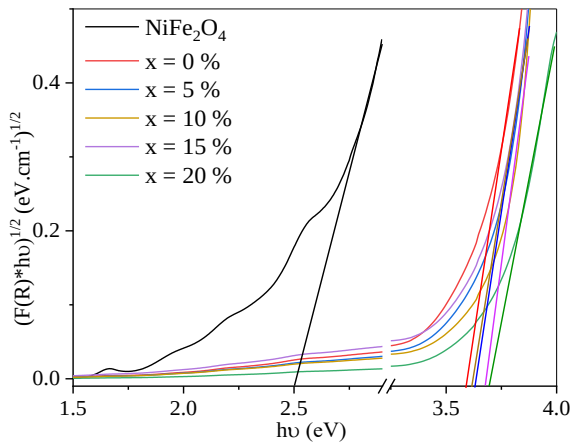

(a)

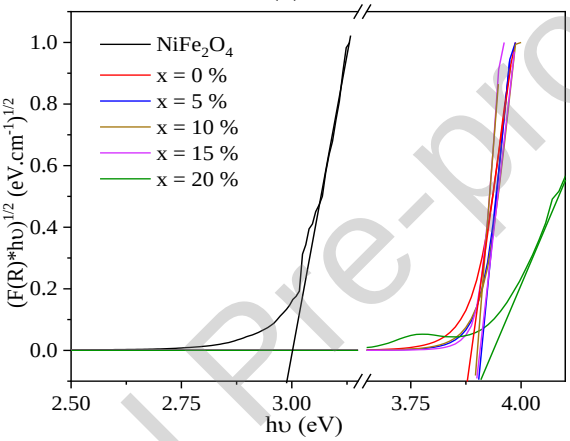

(b)

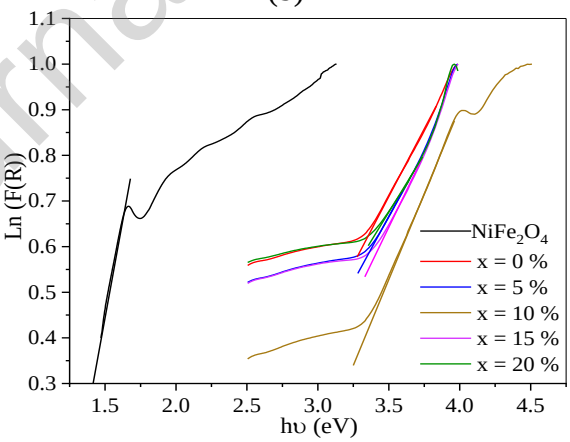

(c)

Figure 8. Variation of the band gap E_g (a) indirect, (b) direct and (c) variation of Urbach energy E_U.

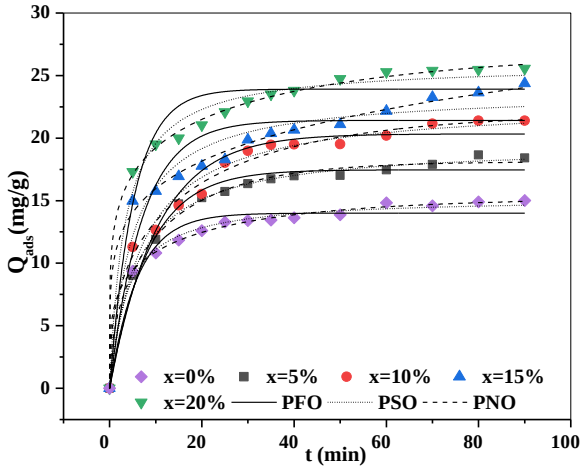

Figure 9. Adsorption of MB on $NiFe_2O_4$-TiO_2/rGO_x, experimental points and their fitting curves.

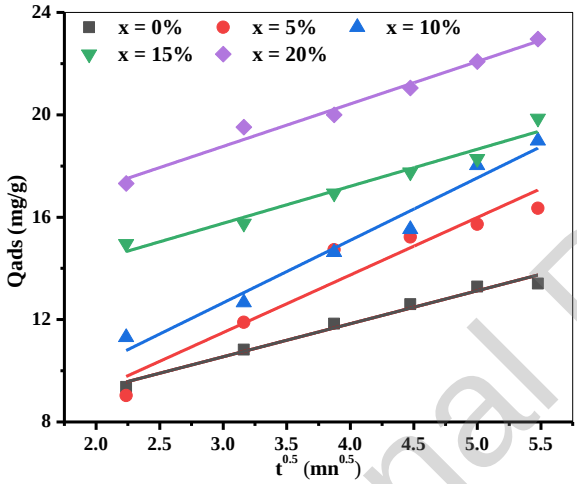

Figure 10. Experimental (symbols) and calculated data (continuous lines) by means of intraparticle diffusion model for MB adsorption onto $NiFe_2O_4$-TiO_2/rGO_x.

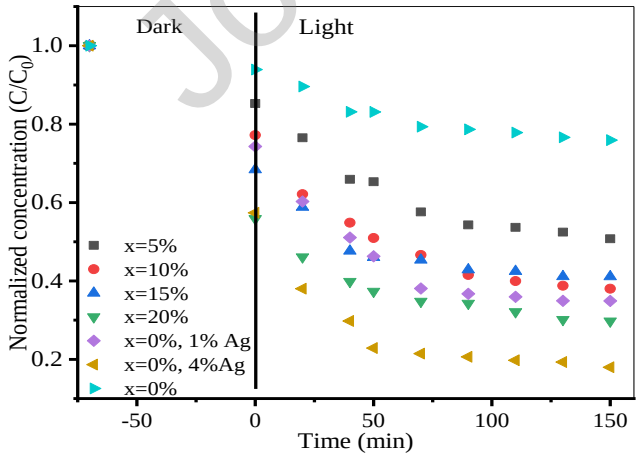

Figure 11. Photodegradation of MB under visible light, experimental and fitted curves.

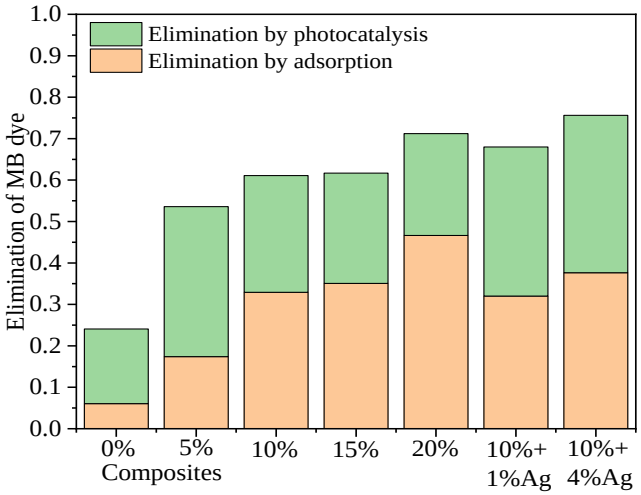

Figure 12. Yield of elimination of MB by adsorption and photocatalysis.

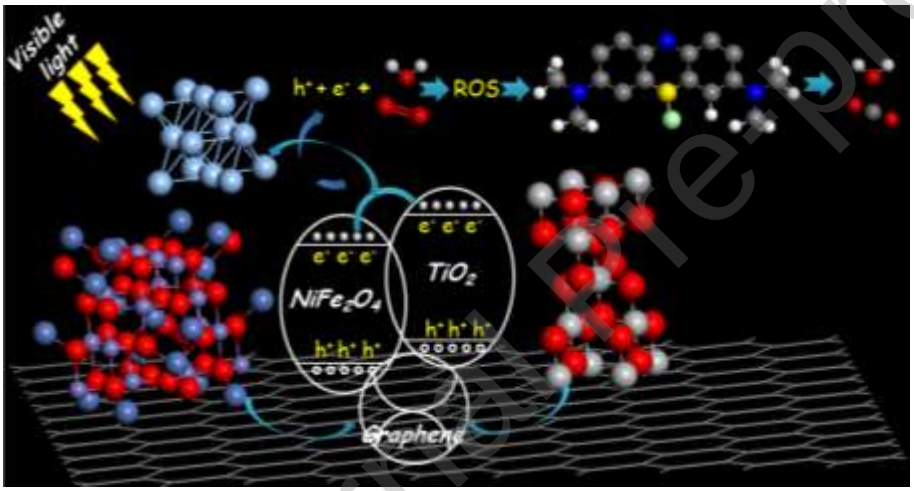

Figure 13. Schematic illustration of the photocatalytic mechanism of $NiFe_2O_4/TiO_2$@Ag composite.

Table captions

Table 1. Lattice parameters, grain sizes, microconstraints and dislocation densities of $NiFe_2O_4$, TiO_2 and $NiFe_2O_4$-TiO_2/rGO_x (x = 0. 5. 10. 15 and 20%).

Single						
TiO_2	a (Å)	3.793				
	c (Å)	9.4929				
	D (Å)	99.57				
$NiFe_2O_4$	a (Å)	8.3471				
	D (Å)	192.59				
$NiFe_2O_4$-TiO_2/rGO_x		0%	5%	10%	15%	20%
TiO_2	a (Å)	3.8017	3.800	3.7955	3.7954	3.7918
	c (Å)	9.5512	9.5395	9.5317	9.5239	9.5200
	D (Å)	86.60	78.76	77.01	76.90	73.77
	ε %	0.940	1.021	1.052	1.059	1.100
	$\delta(nm)^{-2}.10^{-3}$	0.133	0.165	0.168	0.169	0.183
$NiFe_2O_4$	a (Å)	8.3518	8.3446	8.3373	8.339	8.3337

Table 2. Experimental maxima of the adsorbed quantities and modeling results of MB onto $NiFe_2O_4$-TiO_2/rGO_x.

	Q_{exp} (mg/g)	**PFO**			**PSO**			**$Pn^{th}O$**			
		Q_e (mg/g)	R^2	K_1	Q_e (mg/g)	R^2	K_2	Q_e (mg/g)	R^2	n	K_n
x=0%	14.89	14.12	0.927	0.165	15.24	0.997	0.0177	15.96	0.994	2.40	0.006
x=5%	18.65	17.46	0.981	0.118	19.48	0.996	0.0087	19.45	0.996	2.00	0.009
x=10%	21.39	20.33	0.953	0.096	22.85	0.982	0.0062	23.00	0.983	2.12	0.005
x=15%	23.63	21.41	0.888	0.141	23.71	0.956	0.0089	25.01	0.966	2.63	0.001
x=20%	25.46	23.92	0.942	0.191	25.92	0.985	0.0118	28.02	0.992	2.85	0.009

Table 3. Comparison of AIC and R^2 of the models used in this work (adsorption kinetics of MB on $NiFe_2O_4$-TiO_2/rGO_x).

	PFO		**PSO**		**PNO**	
	R^2	AIC	R^2	AIC	R^2	AIC
x=0%	0.927	00.55	0.997	-22.950	0.994	-23.38
x=5%	0.981	-03.40	0.996	-25.780	0.996	-21.73
x=10%	0.953	13.81	0.982	00.075	0.983	03.56
x=15%	0.888	27.11	0.956	14.170	0.966	14.30
x=20%	0.942	20.44	0.985	01.470	0.992	-03.46

Table 4. Intraparticle diffusion model of adsorption of methylene blue MB, on the various composites.

Parameters	**Intraparticle diffusion**				
C (mg/g)	6.68	4.75	5.33	11.42	13.79
K_{id} (mg/gmin$^{0.5}$)	1.29	2.25	2.44	1.45	1.66
R^2	0.981	0.926	0.971	0.963	0.983

Table 5. Apparent rate constants of photocatalysis.

x	**0%**	**5%**	**10%**	**15%**	**20%**	**1%Ag**	**4%Ag**
$K_{ap}10^{-3}$ (min^{-1})	2.66	5.73	8.62	8.28	8.34	9.52	17.88
R^2	0.988	0.992	0.993	0.996	0.996	0.999	0.995

Credit author statement

Riadh Bourzami	Materials synthesis and analysis
Mohamed Khalil GUEDIRI	Adsorption part
Derradji CHEBLI	Photocatalysis part
Abdallah BOUGUETTOUCHA	Photocatalysis part
Abdeltif AMRANE	Materials analysis

Declaration of interests

☒ The authors declare that they have no known competing financial interests or personal relationships that could have appeared to influence the work reported in this paper.

☐The authors declare the following financial interests/personal relationships which may be considered as potential competing interests:

Highlights

- rGO, spinel $Fe_{2.02}Ni_{1.01}O_{3.22}$, anatase $TiO_{2,}$ and metallic Ag nanocrystals were studied
- Nanocrystals and various ratio of rGO form hybrid heterojunction nanocomposites
- High adsorptive and photocatalytic performances for the elimination of BM pollutant
- rGO mass ratio 10% gives the best synergy between the adsorption and photocatalysis
- Photocatalytic mechanism is explained via electronic transfer between the components